



# CHORUS

This is the accepted manuscript made available via CHORUS. The article has been published as:

## Modeling and experimental validation of dynamical effects in Bragg coherent x-ray diffractive imaging of finite crystals

Yuan Gao, Xiaojing Huang, Ross Harder, Wonsuk Cha, Garth J. Williams, and Hanfei Yan

Phys. Rev. B **106**, 184111 — Published 30 November 2022

DOI: [10.1103/PhysRevB.106.184111](https://doi.org/10.1103/PhysRevB.106.184111)

1

2 Title:

3 Modeling and experimental validation of dynamical effect in Bragg  
4 coherent x-ray diffractive imaging from finite crystals

5 Authors:

6 Yuan Gao<sup>1\*</sup>, Xiaojing Huang<sup>1</sup>, Ross Harder<sup>2</sup>, Wonsuk Cha<sup>2</sup>, Garth J.  
7 Williams<sup>1\*</sup>, and Hanfei Yan<sup>1\*</sup>

8 <sup>1</sup>*National Synchrotron Light Source II, Brookhaven National Laboratory,*  
9 *Upton, NY 11973, USA*

10 <sup>2</sup>*Advanced Photon Source, Argonne National Laboratory, Lemont, IL 60439,*  
11 *USA*

12 *\*Email: [yuangao@bnl.gov](mailto:yuangao@bnl.gov); [gwilliams@bnl.gov](mailto:gwilliams@bnl.gov); [hyan@bnl.gov](mailto:hyan@bnl.gov)*

13 Corresponding author:

14 Yuan Gao,  
15 Brookhaven National Laboratory, Building 743, Upton, NY 11973-5000.  
16 Phone 631 344-3781, Email: [yuangao@bnl.gov](mailto:yuangao@bnl.gov)

17 Keywords:

18 X-ray dynamical diffraction, Bragg coherent diffractive imaging

19

## 20 **Abstract:**

21 Bragg coherent diffractive imaging (BCDI) is a non-invasive microscopy technique that can visualize  
22 the shape and internal lattice deviations of crystals with nanoscale spatial resolution and picometer  
23 deformation sensitivity. Its strain imaging capability relies on Fourier transform based iterative phase  
24 retrieval algorithms, which are mostly developed under the kinematical approximation. Such  
25 approximation prohibits the application of BCDI on larger crystals, which are commonly seen in most  
26 emerging functional materials. Understanding the dynamical effect in BCDI, as well as developing a  
27 validated method for modeling BCDI at the dynamical diffraction limit, is crucial for applying BCDI to  
28 hierarchical systems that contain micron-sized crystals and grains. Here we report a comparative study  
29 on the impact of dynamical diffraction effects by comparing the reconstruction results from two  
30 measurements of the same crystal. Forward simulation is implemented to show subtle changes of  
31 interference fringes in the diffraction pattern due to the dynamical diffraction, and is compared directly  
32 with the experimental data.

## 33 **I. Introduction**

34 Strain can strongly influence the mechanical, chemical, and electronic properties of materials. Thus,  
35 precision measurement of crystal strain is a key challenge for characterizing and optimizing emergent  
36 functional materials. Hard x-ray Bragg coherent diffractive imaging (BCDI) has been demonstrated to  
37 be a very powerful tool for imaging lattice deformation in crystalline materials [1–6]. It provides a full-  
38 field type imaging capability to map three-dimensional strain distribution in a micron-sized field of view  
39 with nanometer-scale spatial resolution and picometer-scale deformation sensitivity. In a typical BCDI  
40 measurement, a finite crystal is illuminated by a coherent x-ray beam, and the far-field 3D diffraction  
41 pattern in the vicinity of a single Bragg reflection is recorded with a spatial sampling rate beyond the  
42 Nyquist limit. The acquired 3D diffraction pattern is inverted to a complex object function using phase  
43 retrieval algorithms. Traditionally, the amplitude of the reconstructed object function indicates the  
44 scattering density distribution of the crystal, while the phase represents a projection of the  
45 deformation field to the momentum transfer vector of the measured Bragg peak.

46 Most BCDI phase retrieval algorithms [7–9] are developed under the kinematical approximation, in  
47 which the dynamical effects—namely multiple scattering and extinction—are neglected. With  
48 such simplification, the far-field diffraction intensity from a finite crystal is the modulus square of  
49 the 3D Fourier transform (FT) of its effective electron density and deformation field, while the  
50 inverse FT of the far-field intensity provides an autocorrelation of the object. Therefore, the phase  
51 problem can be efficiently solved via FT-based iterative optimization algorithms, using *a priori*  
52 knowledge that the object being imaged is isolated. Such phase retrieval algorithms have been  
53 successfully applied to various systems, where sizes of measured crystals are typically in the range from  
54 a few hundreds of nanometers to approximately 1 micron. For larger crystals, those algorithms do not  
55 provide a simple map of the electron density, since the kinematical approximation is not valid anymore.  
56 Applying established FT-based algorithms on Bragg diffraction patterns from larger crystals will cause  
57 significant artefacts in both amplitude and phase of the reconstructed complex object functions [10].

58 Theoretically, the dynamical effects can be neglected if the size of a crystal is smaller than the x-  
59 ray extinction length [11,12]. However, in practice, it is difficult to predict whether a crystal can be  
60 treated under the kinematical approximation, since the extinction length of x-ray photons in a  
61 particular crystal could change significantly due to the lattice deformation field. For example, the  
62 extinction length of [111] Bragg diffraction at a photon energy of 9 keV is about 0.25  $\mu\text{m}$  in a  
63 perfectly ordered gold or lead crystal [13]. However, micron-sized gold and lead crystals have been  
64 successfully imaged without any significant artefacts, using BCDI and FT-based phase retrieval

65 algorithms [2,3,14]. The kinematical approximation is still valid in those large crystals, because of  
66 residual lattice deformations associated with the sample preparation. Without knowing the  
67 ground truth, one could easily confuse the artefacts from dynamical effects with actual features  
68 in a crystal far from equilibrium with its environment. Therefore, developing a wave propagation  
69 method that accommodates dynamical effects, as well as the corresponding phase retrieval  
70 approach, is crucial for applying BCDI on large crystals.

71 Dynamical effects can be described in the frame of x-ray dynamical diffraction theory, which has  
72 been extensively developed for decades [11,15–17]. Works have been done to investigate the impact  
73 of dynamical diffraction effect on transmitted beam [18,19] and extended samples [20]. More recently,  
74 Yan et al. [21] and Shabalin et al. [22] have applied the theory on finite crystals to simulate the coherent  
75 diffraction patterns. The latter group also simulated BCDI on a hemispherical Pb particle using the same  
76 diffraction geometry and a similar crystal dimension described in Refs. [3]. While both works provide  
77 valuable insight into the impact of dynamical effects on BCDI, none of them has validated the  
78 simulations against experimental data. In this paper, we perform BCDI measurements of the same  
79 crystal at two energy points to illustrate the impact of dynamical diffraction effects in the  
80 reconstruction, and use forward simulation to validate subtle changes observed in the diffraction  
81 pattern associated with different diffraction modes against experimental data.

## 82 **II. BCDI data collection and phasing**

### 83 **A. BCDI sample preparation and data collection**

84 The gold crystal sample was prepared by dewetting evaporated gold films at a temperature just  
85 below melting [1]. The target crystal was selected based on its dimension and the estimated x-ray  
86 extinction length. According to the database [13], the extinction length in a perfectly ordered gold  
87 crystal is about 0.25  $\mu\text{m}$  for [002] reflection and approximately 0.70  $\mu\text{m}$  for [004] reflection. The  
88 extinction length is calculated assuming a sigma-polarized incident wave. Details about estimation of  
89 the extinction length are discussed in Appendix A. Considering the presence of deformation, these  
90 numbers could be larger in a real crystal. Therefore, we selected a crystal that has a size of  
91 approximately 700 nm in diameter and 350 nm in height. Given its dimensions, the [004] diffraction  
92 patterns measured from this crystal should be inverted correctly using algorithms developed under the  
93 kinematical approximation, while reconstructions from [002] datasets are expected to show significant  
94 artefacts due to dynamical diffraction effects. In the later section of this paper, the reconstruction from  
95 [004] reflection serves as the model of crystal to perform forward simulation, while the [002] reflection  
96 is used as the reference to validate the simulation results.

97 The BCDI experiment was conducted at beamline 34-ID-C of the Advanced Photon Source, Argonne  
98 National Laboratory. The dataset of [002] reflection was collected at a photon energy of 7.5 keV, and  
99 [004] reflection was collected at 15 keV. The two reflections were measured using identical diffraction  
100 geometry, where a pixelated detector with 55  $\mu\text{m} \times 55 \mu\text{m}$  pixels was orientated at  $\delta = 41.40^\circ$  and  $\gamma =$   
101  $26.55^\circ$  (as shown in Fig 1). The crystal was rotated around y-axis during rocking scans, using a rocking  
102 step of 6 mdeg for [002] reflection and 3 mdeg for [004] reflection. The sample-detector distance was  
103 fixed at 1.5 m. As a result, the sampling rate of [004] reflection is slightly below the ideal condition,  
104 while the spatial resolution of reconstructions from [002] reflection is reduced due to the limitation in  
105 the largest scattering angle.

### 106 **B. BCDI Phase retrieval**

107 The collected diffraction datasets were inverted using the established error reduction (ER) and  
108 hybrid input-output (HIO) algorithms [7]. All the phasing processes were initialized using random seeds  
109 and a support size of 80% of the input array. 4500 iterations were carried out for each phasing trial.

110 The first 3600 iterations were switched between 50 iterations of ER and 250 iterations of HIO to  
 111 approach the global minimum. The following 900 iterations were performed with ER only to refine the  
 112 converged solution. Considering the large crystal size and limited beam coherence length, an iterative  
 113 blind-deconvolution method, namely the Richardson-Lucy (RL) algorithm [23,24], was adopted to  
 114 separate the beam coherence function from estimate of the diffracted wavefield [25]. The coherence  
 115 function was updated every 50 iterations starting from the 1200<sup>th</sup> iteration, with RL algorithm runs for  
 116 20 iterations per update. The final object is obtained by averaging over the estimated objects resulting  
 117 from every other iteration in the last 100 iterations.

118 Due to the absorption and extinction effects, part of the reconstructed complex object may have  
 119 much weaker amplitude, which has been discussed in previous theoretical studies [10,22]. Therefore,  
 120 the regular shrink-wrap [26] method often cannot constrain the support correctly, resulting in a cavity-  
 121 or pit-like artefact in the final reconstruction. To avoid this problem, we used an alternative approach  
 122 to shrink the support at a controlled speed. In this approach, the 3D dimensions of support are reduced  
 123 by a certain number of voxels with a specified interval of iterations, and the shrinking stops where the  
 124 boundary of the support touches the boundary of the estimated object, determined by a pre-defined  
 125 threshold. This method allows the algorithms to find the correct solution before stagnating around a  
 126 local minimum due to an overtightened support.

127 Fig. 1 demonstrate the reconstruction and the corresponding error metrics of 7.5 keV data. To avoid  
 128 the potential risk of overtightening the support, the threshold for determining the edge of crystal was  
 129 set to approximately 5% in the 1<sup>st</sup> trial of phase retrieval. The resultant amplitude and phase of the  
 130 retrieved object function are shown in Fig. 1a. Although the boundary of the crystal can be easily  
 131 distinguished by eye, the region between the edge of the intentionally loosed support and the edge of  
 132 the crystal contains voxels with relatively large amplitudes. To get a clean morphology of the crystal,  
 133 we conducted a second trial of phase retrieval, using a fixed support that was obtained by thresholding  
 134 the first reconstruction followed by manual modification. The fixed-support phase retrieval gave a  
 135 reconstruction with well-defined crystal boundary. Fig. 1b shows slices of amplitude of the retrieved  
 136 object function along the three axes of lab frame Cartesian coordinate, respectively. As the x-ray wave  
 137 was incident along +z axis and diffracted in the outboard-upward direction, the downstream part of  
 138 the crystal has lower amplitude compared to the remaining part. The corresponding slices of phase  
 139 demonstrate unphysical artefacts that are spatially correlated to the low-amplitude part, suggesting  
 140 that they are originated from the absorption and extinction effects of the x-rays. It is also worth noting  
 141 that the phase artefacts are not linearly proportional to the optical path of x-ray inside the crystal,  
 142 indicating the presence of the extinction effect [10]. Two error metrics were used to monitor the  
 143 convergence of the phase retrieval algorithm. Besides the traditional reciprocal-space  $\chi^2$ -squared error  
 144 metric, an  $\eta^2$ -squared error metric was used to measure the iteration-to-iteration variation.  $\eta^2$  is defined  
 145 as:

$$152 \quad \eta^2 = \frac{|\mathcal{F}(o_n) - \mathcal{F}(o_{n-1})|^2}{|\mathcal{F}(o_{n-1})|^2}$$

146 where  $o_n$  is the estimate of the complex object on  $n^{\text{th}}$  iteration. Fig. 1d demonstrates the error metrics  
 147 during two phase retrieval trials. Both trials have final  $\chi^2$  values below  $10^{-2}$ , suggesting a reliable phase  
 148 retrieval result. The 2<sup>nd</sup> trial ends at a slightly higher  $\chi^2$  value, which is likely due to fixing the support.  
 149 As for the  $\eta^2$  values, the 1<sup>st</sup> trial stagnates around  $10^{-3}$  during the last 900 iterations of ER, indicating  
 150 the algorithm was trapped in a local minimum due to the intentionally loosed support. As a comparison,  
 151 the 2<sup>nd</sup> trial was able to converge to a consistent result, with a final  $\eta^2$  value below  $10^{-8}$ .

153 Same phase retrieval procedure was used for the 15 keV dataset, i.e., a loose-support phase retrieval  
 154 followed by a fixed-support one. As mentioned previously, the extinction length of [004] diffraction  
 155 from a perfectly ordered Au crystal is about 0.70  $\mu\text{m}$ , similar to or larger than the dimensions of the  
 156 crystal we measured. Therefore, we estimated that kinematical approximation is still valid for the 15  
 157 keV dataset. The result of phase retrieval confirmed this estimation. Fig. 2a shows only the amplitude  
 158 and phase of object reconstructed using a fixed support. Comparing with the 7.5 keV dataset, the

159 reconstruction from 15 keV dataset has an almost identical morphology, with a relatively smooth  
 160 amplitude distribution inside the crystal boundary, as expected. The corresponding phase maps show  
 161 a smooth distribution in the center part of the crystal, while the region near the boundary has an  
 162 approximately 1.2 radian phase ramp relative to the center. This indicates the presence of lattice  
 163 displacement in the surface layers of the crystal, which has been discussed in previous studies [2,14].  
 164 The corresponding  $\chi^2$  and  $\eta^2$  error metrics (see Fig. 2b) have final values below  $10^{-2}$  and  $10^{-8}$ ,  
 165 respectively, which are as good as the 2<sup>nd</sup> trial of 7.5 keV case.

### 166 III. Forward simulation of dynamical diffraction

167 In the first part of this section, we briefly describe the formulism used for propagating the x-ray  
 168 wave field through a crystal in the dynamical diffraction regime. Then, the crystal model reconstructed  
 169 from the 15 keV dataset is used as the ground truth to simulate the far field diffraction patterns of two  
 170 Bragg peaks at corresponding photon energies. The simulation results are validated by a direct  
 171 comparison with the experimental data.

#### 172 A. Dynamical diffraction formulism

173 The simulation method used in this work is developed based on the study conducted by Yan et  
 174 al. [21], with some modifications inspired by Ref. [22]. The propagation and interaction of wavefields  
 175 inside a crystal, as well as the absorption and refraction effects, are described by the Takagi-Taupin  
 176 equations (TTE) [15,16]. Following Ref. [21,22,27], the crystal wave with two-beam approximation can  
 177 be written as:

$$182 \quad \begin{aligned} \frac{\partial D_0}{\partial s_0} &= \frac{ik}{2} (\chi_0 D_0 + \chi_{\bar{h}} D_h) \\ \frac{\partial D_h}{\partial s_h} &= \frac{ik}{2} \left\{ \chi_h D_0 + \left[ 1 + \chi_0 - \frac{k_h^2}{k^2} + \frac{2}{k} \frac{\partial(\mathbf{h} \cdot \mathbf{u})}{\partial s_h} \right] D_h \right\} \end{aligned} \quad (1)$$

178 where  $\hat{\mathbf{s}}_0$  and  $\hat{\mathbf{s}}_h$  are the unit vectors along the transmitted wave,  $D_0(\mathbf{r}) \exp(i\mathbf{k}_0 \cdot \mathbf{r})$ , and diffracted  
 179 wave,  $D_h(\mathbf{r}) \exp(i\mathbf{k}_h \cdot \mathbf{r} - i\mathbf{h} \cdot \mathbf{u})$ , respectively;  $k = \frac{2\pi}{\lambda}$  is the wavevector of x-ray, and  $\mathbf{k}_0 = k\hat{\mathbf{s}}_0$ ,  
 180  $\mathbf{k}_h = \mathbf{k}_0 + \mathbf{h} = k_h\hat{\mathbf{s}}_h$ ;  $\mathbf{h}$  is the reciprocal lattice vector of the unstrained crystal;  $\mathbf{u}$  is the displacement  
 181 vector;  $\chi_0$ ,  $\chi_h$ , and  $\chi_{\bar{h}}$  are Fourier coefficients of the susceptibility function of the crystal.

183 Eq. 1 are coupled partial-differential equations and can only be solved analytically in some particular  
 184 cases [12]. For a general case, it is necessary to integrate the equations numerically. An iterative  
 185 process is developed to numerically solve Eq. 1. For an incident wave  $\psi_0(\mathbf{r}) \exp(i\mathbf{k}_0 \cdot \mathbf{r})$ , at  $n^{\text{th}}$   
 186 iteration, the transmitted and diffracted waves at an arbitrary point  $(s_0, s_h)$  on an  $\hat{\mathbf{s}}_0$ ,  $\hat{\mathbf{s}}_h$  slice of the  
 187 crystal (see Fig. 3a) can be obtained:

$$194 \quad D_0^{(n)}(s_0, s_h) = D_0(s_0^\Gamma, s_h) \exp[ic_0(s_0 - s_0^\Gamma)] + ic_{\bar{h}} \int_{s_0^\Gamma}^{s_0} D_h^{(n-1)}(s'_0, s_h) \exp[ic_0(s_0 - s'_0)] ds'_0 \quad (2)$$

$$195 \quad D_h^{(n)}(s_0, s_h) = ic_h \int_{s_h^\Omega}^{s_h} D_0^{(n)}(s_0, s'_h) \exp\{i\mathbf{h} \cdot [\mathbf{u}(s_0, s_h) - \mathbf{u}(s_0, s'_h)] + ic_w(s_h - s'_h)\} ds'_h \quad (3)$$

188 where  $c_{0,h,\bar{h}} = \frac{1}{2} k \chi_{0,h,\bar{h}}$  and  $c_w = \frac{1}{2} k \left( 1 + \chi_0 - \frac{k_h^2}{k^2} \right)$ . The integrations use boundary conditions  
 189  $D_0(s_0^\Gamma, s_h) = \psi_0(s_0^\Gamma, s_h)$  and  $D_h(s_0, s_h^\Omega) = 0$ , where  $\psi_0$  is the incident x-ray wave. As shown in Fig. 3a,  
 190  $\Gamma$  and  $\Omega$  are the upstream crystal boundaries of the transmitted and diffracted waves, respectively;  $s_0^\Gamma$   
 191 is the  $s_0$  coordinate of  $\Gamma$  at  $s_h$ , and  $s_h^\Omega$  is the  $s_h$  coordinate of  $\Omega$  at  $s_0$ . The iteration starts by assuming  
 192  $D_h^{(0)} = 0$ , and continues until a converged solution emerges. The mathematical proof of convergence  
 193 is detailed in Ref. [22].

196 For a specific diffraction geometry, Eq. 2,3 are numerically solved for each  $\hat{\mathbf{s}}_0$ ,  $\hat{\mathbf{s}}_h$  slice of the crystal  
 197 to obtain  $D_h$  at the exit boundary of the crystal, yielding a 2D wavefront at the exit crystal surface of

198 the diffracted beam. Such exit wavefront is propagated to far-field using 2D FT, and the resultant  
199 modulus represents the diffraction pattern recorded by a pixelated detector. To simulate a rocking  
200 curve scan, the process described above is repeated at each rocking angle.

201 It is worth mentioning that Eq. 2,3 can also accommodate diffraction with only the absorption and  
202 refraction effects—i.e., ignoring the extinction effect—and the situation at the kinematic limit. One  
203 could easily see that the extinction effect is described by the second term on the right-hand side of Eq.  
204 2: the  $D_0$  propagated from the incident surface  $\Gamma$  to a point  $(s_0, s_h)$  is further attenuated due to the  
205 presence of non-zero  $D_h$  on the propagation path. To neglect this effect, we can simply take the  $D_h$   
206 obtained from the first iteration and propagate it to the far-field. As for the situation at the kinematic  
207 limit, not only is the extinction effect neglected, but also the susceptibilities  $\chi_{0,h,\bar{h}}$  are set to very small  
208 non-zero values. In this case,  $D_h$  in Eq. 3 is simply a function of  $\int D_0(\mathbf{r}) \exp[i\mathbf{h} \cdot \mathbf{u}(\mathbf{r})] d\mathbf{r}$ , which is the  
209 well-known formula of kinematical diffraction.

## 210 **B. Forward simulation of [004] peak**

211 As mentioned earlier in this paper, the [004] diffraction should not see significant dynamical effect,  
212 since the estimate extinction length is comparable to or even larger than the dimension of the crystal.  
213 Therefore, we start with the simulation of [004] diffraction at 15 keV to establish the baseline.

214 The reconstruction from the 15 keV dataset was used as the model for forward simulation. As shown  
215 in Fig. 2a, the amplitude of the reconstructed object contains obvious modulations. These modulations  
216 are commonly seen in BCDI and usually attributed to numerical errors induced by the FT-based iterative  
217 phase retrieval. To remove such unphysical features, the amplitude inside the crystal was set to 1,  
218 where the crystal boundary was determined by an iso-surface level of 20%.

219 Three types of far-field diffraction patterns were calculated: a dynamical diffraction model (DM), a  
220 kinematical diffraction model with absorption and refraction effects (AR), and a pure kinematical  
221 diffraction model (KA). The simulations were normalized using integrated intensity of the experimental  
222 data. All simulated diffraction patterns were aligned to the data by minimizing the cross-correlation  
223 coefficient between each pair of 3D diffraction patterns.

224 Fig. 3 demonstrates the experimental data and results of all three models. Logarithmic-scale line  
225 intensity variations across the center of the Bragg peak are plotted along the three axes of diffraction  
226 patterns in detector frame, as shown in Fig. 3c. As expected, simulations from three models show very  
227 similar intensity profiles, since the effects of absorption, refraction, and extinction are negligible for  
228 this particular reflection. Compared to the data, all three models correctly reproduce the measured  
229 intensity distribution down to the order of  $10^{-4}$ , with well-matched interference fringes. The  
230 simulations slightly differ from the data in the high-q region, especially for where the relative intensity  
231 is less than  $10^{-4}$  of the center of Bragg peak. This phenomenon will be discussed later.

232 Besides the inconsistency in high-q region, simulations also show better fringes visibility when  
233 compared with the data. This is likely an effect of the limited coherence of incident x-ray beam, since  
234 the simulations were conducted assuming the crystal is illuminated by fully coherent beam. Although  
235 this partial coherence effect has been separated from the reconstructed object via blind deconvolution  
236 during the phase retrieval process, it cannot be added back by a simple convolution in the forward  
237 simulation. Technically, the diffraction with a partially-coherent beam should be simulated by  
238 considering all major coherent modes of the beam [28,29]. However, understanding the coherence  
239 property of source at 34-ID-C, as well as performing and validating the decomposition of coherent  
240 modes, is out of the scope of this work. Therefore, partial coherent effect is not accommodated in  
241 forward simulations presented in this paper.

## 242 **C. Forward simulation of [002] peak**

243 Simulation of [002] diffraction at 7.5 keV was conducted using the same method described above.  
244 Similarly, three diffraction models were calculated. It is important to note that the crystal model is

245 retrieved from the [004] dataset since it is more error-free and closer to the ground-truth. The phase  
246 of the reconstructed complex object function represents  $\mathbf{h}_{[004]} \cdot \mathbf{u}$ . When simulating [002] diffraction,  
247 the phase needs to be divided by 2 to match the momentum transfer vector  $\mathbf{h}_{[002]}$ .

248 Simulations were normalized and aligned to the experimental data using the procedure described  
249 in the previous section. In Fig. 4, logarithmic-scale line intensity variations of the simulated diffraction  
250 patterns are plotted against the measured diffraction data. Unlike [004], the KA model result of [002]  
251 is significantly different from ones of DM and AR models. Such differences suggest that absorption,  
252 refraction, and extinction effects play an important role for this reflection.

253 Compared to the data, all models accurately reproduce the height and width of the center peak, but  
254 show different performances in the side lobes. Along the horizontal axis of detector (Fig. 4b), results  
255 from all three models show interference fringes with periodicities and relative intensities similar to the  
256 data. The DM model shows a slightly better consistency, especially on the  $+\Delta q$  side of the center peak.  
257 Like the [004] case, the fringe visibilities of simulated results are better than the data, which can be  
258 attributed to the effect of partial coherence. Along the vertical axis of detector (Fig. 4a), different levels  
259 of consistency are observed on the  $+\Delta q$  side and  $-\Delta q$  side. On the  $+\Delta q$  side, the relative intensities of  
260 side lobes from DM and KA models are very similar to those of data, except for the 2<sup>nd</sup> and 5<sup>th</sup> orders.  
261 For AR model, the 1<sup>st</sup> order side lobe has a relative intensity 30% lower than the one of experimental  
262 data, indicating it cannot reproduce the relative intensity accurately. On the  $-\Delta q$  side, relative  
263 intensities of side lobes calculated from KA model are significantly weaker than those of data by a  
264 factor of 50% or more. The first two side lobes from AR model have similar relative intensities as the  
265 ones of data, but the 3<sup>rd</sup> order is as weak as the one from KA model. As a comparison, DM model  
266 correctly reproduces the intensities of the first three orders of side lobes, down to a relative intensity  
267 as low as  $10^{-4}$ . Higher order side lobes of DM simulation do not match the data very well, which will be  
268 discussed in next section.

269 Besides the visual inspection, we also calculated the  $\chi^2$  error metric between the data and  
270 simulations. The  $\chi^2$  values are 0.047 for DM model, 0.064 for AR model, and 0.121 for KA model. Both  
271 DM and AR have significant lower  $\chi^2$  values than KA, suggesting that most of the subtle changes in side  
272 lobes are caused by the absorption and refraction effects. Meanwhile, DM's error is slightly better than  
273 AR, indicating that the extinction effect also play an important role in this reflection. As a comparison,  
274 for the [004] reflection at 15 keV, the  $\chi^2$  values are 0.081, 0.080, and 0.167 for DM, AR, and KA models,  
275 respectively. While the absorption and refraction effects are still important for [004] reflection, the  
276 difference caused by extinction effect is negligible.

## 277 IV. Discussion

278 As mentioned above, simulations using DM model can accurately reproduce the intensity  
279 distribution in the low-q region, but difference in the high-q region is still observed. This is mostly  
280 caused by two factors. First, because of the well-known  $Q^{-4}$  power-law decay of the diffraction  
281 signal [30], the measured diffraction data has many fewer photon counts in the high-q region. Such  
282 low counts result in a much higher uncertainty of measurement—namely the Poisson noise—as  
283 demonstrated by the error bars in Fig 3c and 4. The weak signal is also more susceptible to background  
284 noise like scattering from alien scatterers [31]. Since we did not add any noise to the simulated  
285 diffraction patterns, it is not surprising that the simulations and data are inconsistent in the high-q  
286 region. Second, we do not know the ground truth and the reconstructed crystal from [004] dataset  
287 could still contain artificial fine structures because of the noisy high-q data. Forward simulations from  
288 such an imperfect crystal model would inherently cause inconsistency in the high-q region when  
289 compared with experimental data.

290 Besides the differences in high-q region, simulations also show mismatch at some specific  
291 momentum transfer values. For example, as shown in Fig. 4a, the 2<sup>nd</sup> side lobe on the  $+\Delta q$  side always  
292 has a much higher relative intensity when comparing simulations to the data. Although the actual



293 cause is unclear, mismatch at a specific momentum transfer value usually indicates the real space  
294 object contains artefacts with the corresponding spatial frequency. Our hypothesis is that the FT-based  
295 phase retrieval process introduces numerical errors with certain spatial frequencies. As shown in Fig.  
296 2a, not only the amplitude of the reconstructed object function contains unphysical modulations, but  
297 the phase term also shows visible modulations that are spatially correlated to those in amplitude. The  
298 modulations in amplitude have been removed before performing forward simulations, based on a  
299 physical assumption that the effective electron density of the crystal is uniform. The phase artefacts,  
300 however, cannot be corrected without knowing the ground truth. A potential solution to this problem  
301 is performing phase retrieval with constrained amplitude variation. Such an additional constraint might  
302 force the algorithm to find a solution with uniform amplitude distribution and eliminate the unphysical  
303 modulations in phase.

304 From the reconstruction of [002] shown in Fig. 1a,b, as well as the previous theoretical  
305 studies [10,22], we can see that both absorption/refraction effect and extinction effect can cause the  
306 low-intensity region in amplitude map and the corresponding phase artefacts. However, these two  
307 effects have different impacts in practice. Absorption/refraction effect induces artefacts that are  
308 linearly proportional to the optical path of x-ray inside the crystal. Such artefacts can be identified and  
309 numerical corrected after the phasing process since the FT-based mathematical model is still valid [10].  
310 As a comparison, extinction effects usually induce non-linear artefacts due to the fact that 3D Fourier  
311 transform is no longer sufficient to describe the physical process. Without knowing the ground truth,  
312 it is very difficult or almost impossible to distinguish the extinction-induced artefacts from actual  
313 deformations in the crystal. The forward simulation method described in this paper can serve as a  
314 validation tool to evaluate the severity of the issue. By comparing simulated diffraction patterns from  
315 kinematical and dynamical models with measured ones, as well as the reconstructions from various  
316 models and measured data (as shown in Appendix B), we can verify whether the reconstruction result  
317 is free from dynamical artefacts.

## 318 **V. Conclusion**

319 In summary, we performed BCDI measurements at two energy points on the same Au crystal to  
320 evaluate the impact of dynamical diffraction in the reconstruction. They correspond to two scenarios:  
321 one where the extinction length is much less than the dimension of crystal, and the other where the  
322 extinction length is comparable to the dimension of crystal. For the former scenario, both dynamical  
323 and kinematical models produce the similar 3D diffraction intensity consistent with measured data,  
324 suggesting that the dynamical effects are negligible. For the latter scenario, simulation using the  
325 dynamical diffraction model reproduces more accurately subtle the subtle changes of the interference  
326 fringes in the experimental data, which cannot be achieved using the kinematical approach. We show  
327 that these subtle changes in the diffraction pattern can lead to erroneous reconstruction result with a  
328 FT-based phase-retrieval algorithm. To alleviate the dynamical artefact, a high-index reflection with  
329 bigger extinction depth would be preferred. The reconstruction-forward simulation method proposed  
330 here can be used as a cross-validation tool to assess the correctness of FT-based model. Although at  
331 the current stage a quantitative correction removing the dynamical artefacts has not been achieved,  
332 the iterative nature of the forward modeling makes it possible to be incorporated into the iterative  
333 optimization algorithm in the future to accommodate dynamical diffraction effects in BCDI phase  
334 retrieval. Such algorithm will enable BCDI on hierarchical systems that contain large crystalline grains  
335 and domains, which are commonly seen in emerging functional materials like additive manufactured  
336 metals, single-crystal cathode materials, and photonic nanostructures. Quantitatively mapping strain in  
337 these systems is essential for understanding and optimizing their functional properties.  
338

## 339 Acknowledgements

340 This research used resources of the National Synchrotron Light Source II, a U.S. Department of Energy  
 341 (DOE) Office of Science User Facility operated for the DOE Office of Science by Brookhaven National  
 342 Laboratory under Contract No. DE-SC0012704. The data of X-ray diffraction experiments were collected  
 343 at the Microdiffraction and Coherent X-ray Scattering beamline 34-ID-C at the Advanced Photon Source,  
 344 a U.S. Department of Energy (DOE) Office of Science User Facilities operated for the DOE Office of  
 345 Science by Argonne National Laboratory under Contract No. DE-AC02-06CH11357.  
 346

## 347 Appendix A: Estimation of extinction length in a finite crystal

348 In this work, the extinction length in a finite crystal is estimated by calculating the extinction depth  
 349 in a perfectly ordered crystal, considering the symmetric case of Bragg geometry. The extinction depth  
 350 is defined as the depth along the normal direction of the surface at which the transmission intensity  
 351 decreased to  $1/e$ . According to Ref. [12], the extinction length in Bragg geometry is

$$360 \quad L_{ext}^{Bragg} = \frac{\lambda \sqrt{\gamma_0 |\gamma_h|}}{\text{Re}(\sqrt{\chi_h \chi_{\bar{h}}})}$$

352 where  $\gamma_{0,h}$  are the direction cosines, and  $\chi_{h,\bar{h}} = \chi_{rh,r\bar{h}} + i\chi_{ih,i\bar{h}}$  are the Fourier components of the  
 353 dielectric susceptibility. Considering the symmetric case, the extinction depth is

$$361 \quad L_{ext}^{Bragg} = \frac{\lambda \sin \theta_B}{\text{Re}(\sqrt{\chi_h \chi_{\bar{h}}})}$$

354 where  $\theta_B$  is the Bragg angle. Also from Ref. [12], there is

$$362 \quad \text{Re}(\sqrt{\chi_h \chi_{\bar{h}}}) = |\chi_{rh}| = \frac{R \lambda^2 F_{rh}}{\pi V}$$

355 where  $R$  is the classical radius of the electron,  $F_h = F_{rh} + iF_{ih}$  is the structure factor, and  $V$  is the  
 356 volume of the unit cell. Combining these two equations, we have

$$363 \quad L_{ext}^{Bragg} = \frac{\lambda \sin \theta_B}{\text{Re}(\sqrt{\chi_h \chi_{\bar{h}}})} = \frac{\pi V \sin \theta_B}{\lambda R F_{rh}} \sim \frac{1}{d}$$

357 where the Bragg's law  $\lambda = 2d \sin \theta_B$  is used. From this equation, we can see that for the symmetric  
 358 case in Bragg geometry, if the photon energy is not very close to the absorption edge, the extinction  
 359 depth has a linear dependence to  $1/d$ .

364 The extinction depths of [002] and [004] reflections at two photon energies in a perfectly ordered  
 365 gold crystal are listed in Table A1. We can see that [002] reflection at 7.5 keV and [004] reflection at 15  
 366 keV have the identical diffraction geometry but significantly different extinction depths. Therefore, we  
 367 are able to tune the ratio between the extinction depth and the crystal size, without changing the  
 368 sample crystal or the diffraction geometry.  
 369

370 **TABLE A1.** Extinction depths of [002] and [004] reflections at 7.5 keV and 15 keV, respectively.

Au	Reflection	Symmetric, Bragg geometry extinction depth [μm]	
		σ-polarized	π-polarized
7.5 keV	[002]	0.251	0.374
	[004]	0.706	2.245
15 keV	[002]	0.251	0.273
	[004]	0.703	1.047

371

## 372 **Appendix B: Phase retrieval of simulated data with different** 373 **models**

374 To better understand the impact of absorption, refraction, and extinction effects on a reconstruction  
375 from diffraction data, we performed phase retrieval on diffraction data simulated using three models.  
376 The results are demonstrated in Fig. A1. For all phasing processes, 4500 iterations were carried out,  
377 while the first 3600 iterations alternated between 50 iterations of ER and 250 iterations of HIO, and  
378 the rest 900 iterations were ER only.

379 Fig. A1a-c demonstrate reconstructed objects from KA, AR, and DM, respectively, using the regular  
380 shrink-wrap approach with a Gaussian blurry function with 1.0 pixel width and 20% cutoff threshold.  
381 As a comparison, results shown in Fig. A1d-f were retrieved using the two-step approach described in  
382 Section II-B. Apparently, both approaches were able to invert the diffraction from KA correctly, resulting  
383 in reconstructions very similar to the crystal model used for forward simulation (as shown in Fig. A1a,  
384 d). However, it is worth noting that both reconstructions contain amplitude modulations, while the  
385 crystal model has a flat amplitude distribution inside the crystal boundary.

386 Reconstructions from the AR simulation, as shown in Fig. A1b, e, have ununiform amplitude  
387 distribution inside the crystal boundary due to the attenuation of transmitted x-ray beam. The  
388 retrieved crystals are slightly different in shape. Specifically, the XZ cross-section of the crystal inverted  
389 via regular shrink-wrap approach (Fig. A1b middle) has an asymmetrical, hexagonal shape, which is  
390 different from the crystal model used for simulation. This can be attributed to the support that was  
391 overtightened by the shrink-wrap approach. While tweaking the parameters of the Gaussian blurry  
392 function might correct this problem, one could easily overlook such an inconsistency without knowing  
393 the ground truth. As a comparison, the two-step approach correctly retrieved the crystal shape.

394 For the DM simulation, phasing with the shrink-wrap approach was not able to obtain a reasonable  
395 crystal shape due to stagnation. The two-step approach, however, was still able to get the correct shape.  
396 Meanwhile, compared with the reconstruction of AR simulation which shows a relatively smooth phase,  
397 reconstruction of DM simulation contains significant phase artefacts that are spatially correlated with  
398 the artefacts in amplitude distribution. In practice, such phase artefacts are likely to be interpreted as  
399 localized defects, while the ground truth or complementary information is lacking.

400

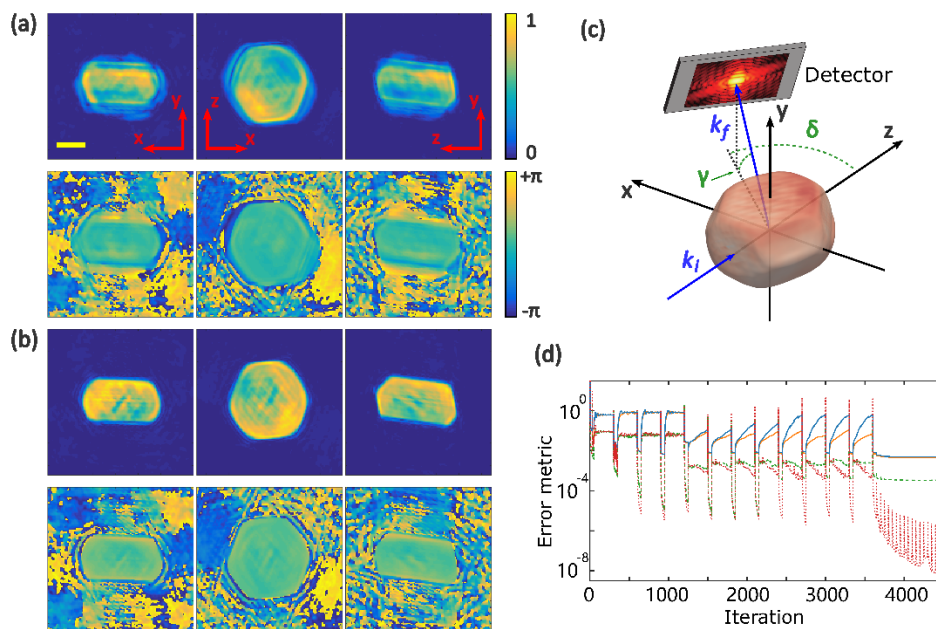
401

## 402 **References**

- 403 [1] I. K. Robinson, I. A. Vartanyants, G. J. Williams, M. A. Pfeifer, and J. A. Pitney, *Reconstruction of the*  
404 *Shapes of Gold Nanocrystals Using Coherent X-Ray Diffraction*, Phys. Rev. Lett. **87**, 195505 (2001).  
405 [2] G. J. Williams, M. A. Pfeifer, I. A. Vartanyants, and I. K. Robinson, *Three-Dimensional Imaging of*  
406 *Microstructure in Au Nanocrystals*, Phys. Rev. Lett. **90**, 175501 (2003).  
407 [3] M. A. Pfeifer, G. J. Williams, I. A. Vartanyants, R. Harder, and I. K. Robinson, *Three-Dimensional*  
408 *Mapping of a Deformation Field inside a Nanocrystal*, Nature **442**, 63 (2006).  
409 [4] I. Robinson and R. Harder, *Coherent X-Ray Diffraction Imaging of Strain at the Nanoscale*, Nature  
410 *Materials* **8**, 291 (2009).  
411 [5] A. Davtyan et al., *Threefold Rotational Symmetry in Hexagonally Shaped Core–Shell*  
412 *(In,Ga)As/GaAs Nanowires Revealed by Coherent X-Ray Diffraction Imaging*, J Appl Cryst **50**, 3  
413 (2017).  
414 [6] S. Labat et al., *Inversion Domain Boundaries in GaN Wires Revealed by Coherent Bragg Imaging*,  
415 *ACS Nano* **9**, 9210 (2015).

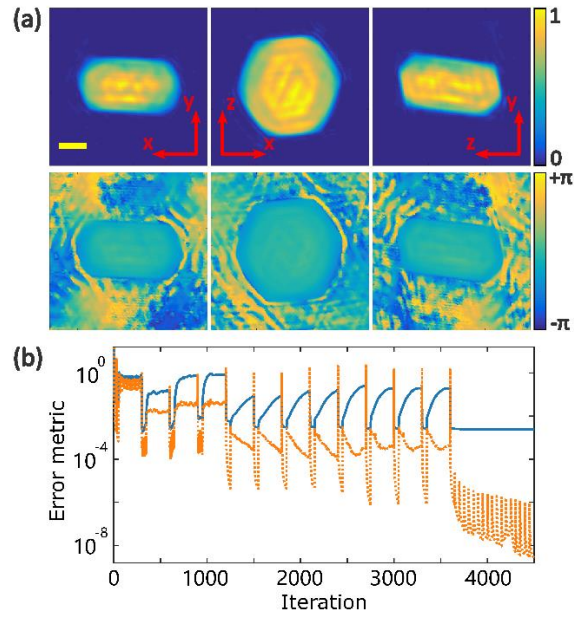
- 416 [7] J. R. Fienup, *Phase Retrieval Algorithms: A Comparison*, Appl. Opt., AO **21**, 2758 (1982).
- 417 [8] V. Elser, *Phase Retrieval by Iterated Projections*, J. Opt. Soc. Am. A **20**, 40 (2003).
- 418 [9] S. Marchesini, *A Unified Evaluation of Iterative Projection Algorithms for Phase Retrieval*, Review  
419 of Scientific Instruments **78**, 011301 (2007).
- 420 [10] W. Hu, X. Huang, and H. Yan, *Dynamic Diffraction Artefacts in Bragg Coherent Diffractive Imaging*,  
421 J Appl Cryst **51**, 167 (2018).
- 422 [11] B. W. Batterman and H. Cole, *Dynamical Diffraction of X Rays by Perfect Crystals*, Rev. Mod. Phys.  
423 **36**, 681 (1964).
- 424 [12] A. Authier, *Dynamical Theory of X-Ray Diffraction* (Oxford University Press, Oxford, 2003).
- 425 [13] S. A. Stepanov, *X-Ray Server: An Online Resource for Simulations of x-Ray Diffraction and Scattering*,  
426 in *Advances in Computational Methods for X-Ray and Neutron Optics*, Vol. 5536 (SPIE, 2004), pp.  
427 16–26.
- 428 [14] R. Harder, M. A. Pfeifer, G. J. Williams, I. A. Vartanyants, and I. K. Robinson, *Orientation Variation*  
429 *of Surface Strain*, Phys. Rev. B **76**, 115425 (2007).
- 430 [15] S. Takagi, *Dynamical Theory of Diffraction Applicable to Crystals with Any Kind of Small Distortion*,  
431 Acta Crystallographica **15**, 1311 (1962).
- 432 [16] D. Taupin, *Théorie dynamique de la diffraction des rayons X par les cristaux déformés*, Bulletin de  
433 Minéralogie **87**, 469 (1964).
- 434 [17] C. R. Wie, T. A. Tombrello, and T. Vreeland, *Dynamical X-ray Diffraction from Nonuniform*  
435 *Crystalline Films: Application to X-ray Rocking Curve Analysis*, Journal of Applied Physics **59**, 3743  
436 (1986).
- 437 [18] O. Yu. Gorobtsov and I. A. Vartanyants, *Phase of Transmitted Wave in Dynamical Theory and Quasi-*  
438 *Kinematical Approximation*, Phys. Rev. B **93**, 184107 (2016).
- 439 [19] M. Civita, A. Diaz, R. J. Bean, A. G. Shabalin, O. Yu. Gorobtsov, I. A. Vartanyants, and I. K. Robinson,  
440 *Phase Modulation Due to Crystal Diffraction by Ptychographic Imaging*, Phys. Rev. B **97**, 104101  
441 (2018).
- 442 [20] A. Pateras, J. Park, Y. Ahn, J. A. Tilka, M. V. Holt, H. Kim, L. J. Mawst, and P. G. Evans, *Dynamical*  
443 *Scattering in Coherent Hard X-Ray Nanobeam Bragg Diffraction*, Phys. Rev. B **97**, 235414 (2018).
- 444 [21] H. Yan and L. Li, *X-Ray Dynamical Diffraction from Single Crystals with Arbitrary Shape and Strain*  
445 *Field: A Universal Approach to Modeling*, Phys. Rev. B **89**, 014104 (2014).
- 446 [22] A. G. Shabalin, O. M. Yefanov, V. L. Nosik, V. A. Bushuev, and I. A. Vartanyants, *Dynamical Effects in*  
447 *Bragg Coherent X-Ray Diffraction Imaging of Finite Crystals*, Phys. Rev. B **96**, 064111 (2017).
- 448 [23] W. H. Richardson, *Bayesian-Based Iterative Method of Image Restoration\**, J. Opt. Soc. Am., JOS A  
449 **62**, 55 (1972).
- 450 [24] L. B. Lucy, *An Iterative Technique for the Rectification of Observed Distributions*, The Astronomical  
451 Journal **79**, 745 (1974).
- 452 [25] J. N. Clark, X. Huang, R. Harder, and I. K. Robinson, *High-Resolution Three-Dimensional Partially*  
453 *Coherent Diffraction Imaging*, Nature Communications **3**, 993 (2012).
- 454 [26] S. Marchesini, H. He, H. N. Chapman, S. P. Hau-Riege, A. Noy, M. R. Howells, U. Weierstall, and J. C.  
455 H. Spence, *X-Ray Image Reconstruction from a Diffraction Pattern Alone*, Physical Review B **68**,  
456 140101 (2003).
- 457 [27] J. Gronkowski, *Propagation of X-Rays in Distorted Crystals under Dynamical Diffraction*, Physics  
458 Reports **206**, 1 (1991).
- 459 [28] O. Chubar and R. Celestre, *Memory and CPU Efficient Computation of the Fresnel Free-Space*  
460 *Propagator in Fourier Optics Simulations*, Opt. Express, OE **27**, 28750 (2019).
- 461 [29] R. Li and O. Chubar, *CPU and Memory Efficient Coherent Mode Decomposition for the Partially*  
462 *Coherent X-Ray Simulations*, in *Advances in Computational Methods for X-Ray Optics V*, Vol. 11493  
463 (SPIE, 2020), pp. 78–87.
- 464 [30] Q. Shen, I. Bazarov, and P. Thibault, *Diffractive Imaging of Nonperiodic Materials with Future*  
465 *Coherent X-Ray Sources*, J Synchrotron Rad **11**, 432 (2004).

466 [31] G. Williams, M. Pfeifer, I. Vartanyants, and I. Robinson, *Effectiveness of Iterative Algorithms in*  
467 *Recovering Phase in the Presence of Noise*, Acta Crystallographica Section A **63**, 36 (2007).  
468



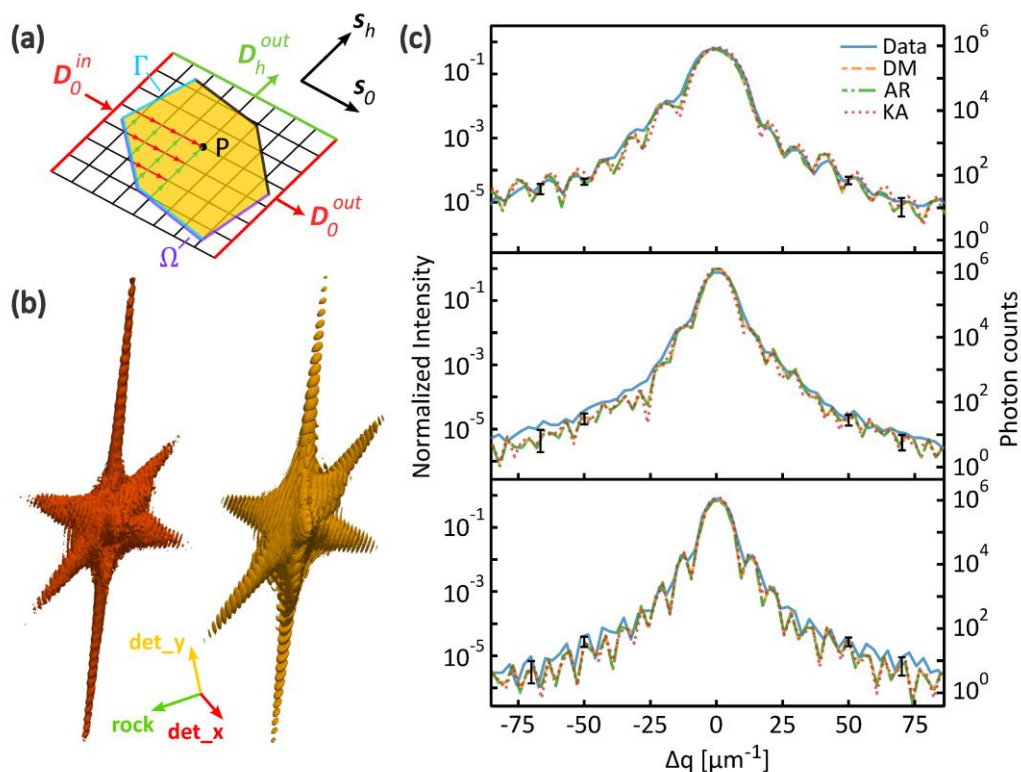
470  
471  
472  
473  
474  
475  
476  
477  
478  
479

**FIG. 1.** Reconstruction from [002] peak at 7.5 keV. The diffraction data was first inverted using an intentionally loosened support (a) and then using a fixed support (b). The scale bar is 250 nm. For both (a) and (b), slices of amplitude (top row) and phase (bottom row) are plotted, where the left, middle, and right columns are the slices along x-y, x-z, and y-z planes, respectively. The definition of diffraction geometry is shown in (c).  $k_i$  and  $k_f$  are the wavevectors of incident and diffracted X-ray photons, respectively. The laboratory coordinate is right-handed, where y is upward, and z is the propagation direction of incident x-ray beam.  $\delta$  and  $\gamma$  are the detector angles. (d) demonstrates error metrics during the iterative phase retrieval.  $\chi^2$  of the first (blue line) and second (amber line) trials, as well as the corresponding  $\eta^2$  (green dashed-line and red dashed-line, respectively), are plotted in logarithmic scale.



480  
 481  
 482  
 483  
 484  
 485  
 486

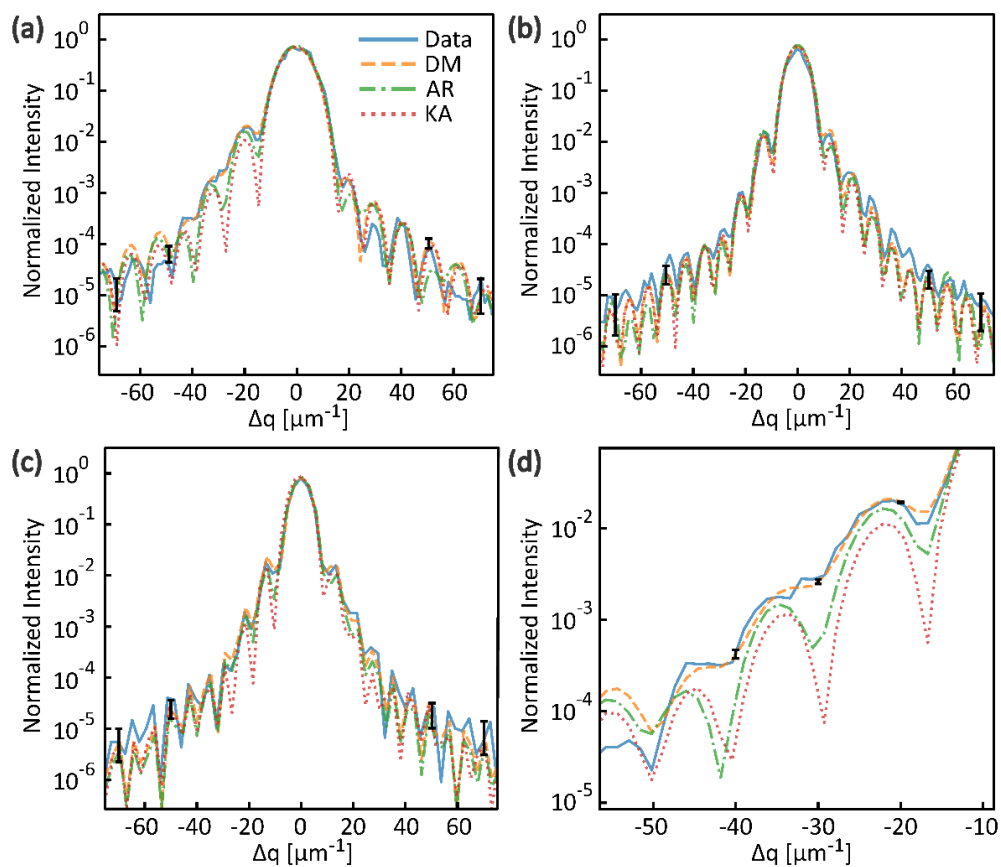
**FIG. 2.** Reconstruction from [004] peak at 15 keV. The diffraction data was inverted following the same two-step procedure. The result using fixed support is shown in (a). The scale bar is 250 nm. Slices of amplitude (top row) and phase (bottom row) are demonstrated, where the left, middle, and right columns are the slices along x-y, x-z, and y-z planes, respectively. Error metrics— $\chi^2$  (solid blue) and  $\eta^2$  (dashed amber)—during the phase retrieval with fixed support are plotted in logarithmic scale in (b).



488  
 489  
 490  
 491  
 492  
 493  
 494  
 495  
 496  
 497  
 498

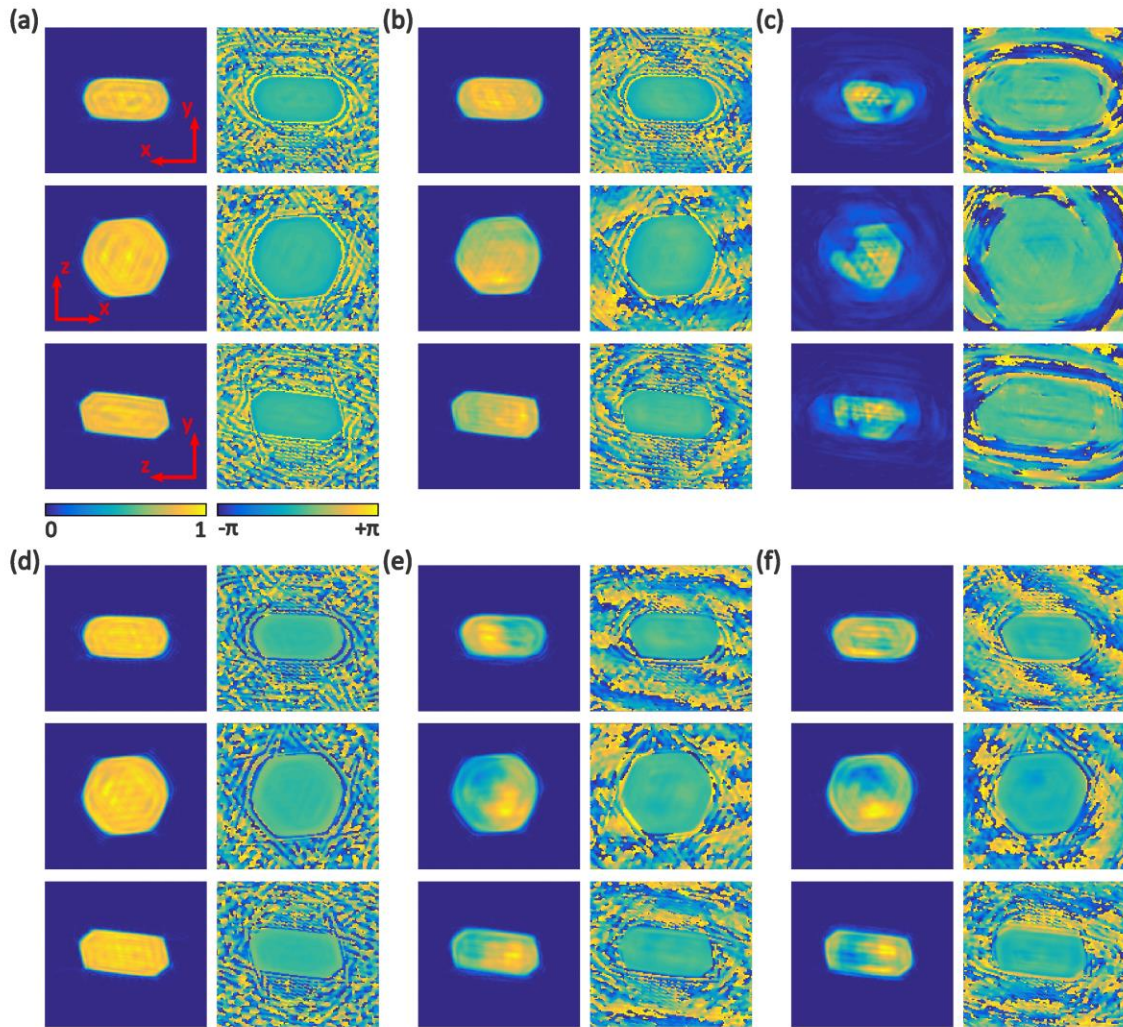
**FIG. 3.** Forward simulation of [004] peak at 15 keV. (a) Schematic of x-ray diffraction from an arbitrary crystal.  $s_0, s_h$  represent the directions of transmitted and diffracted waves, respectively. Boundary conditions must be satisfied on  $\Gamma$  (blue) for transmitted wave and on  $\Omega$  (purple) for diffracted wave. The wavefield at an arbitrary voxel  $P$  inside the crystal is integrated from all upstream voxels, as marked by red and green arrows. (b) 3D diffraction intensity of experimental data (left) and forward simulation from DM model (right), plotted in the detector frame. (c) Line intensity variations across the center of 3D diffraction intensity—along y-axis (top) and x-axis (middle) of detector—and rocking axis (bottom). Simulation results from DM (dashed amber), AR (dashed green), and KA (dashed red) are normalized to the experimental data (solid blue) by integrated intensity, and then aligned together using cross-correlation. Black error bars represent the Poisson noise of DM model simulation at  $\pm 50$  and  $\pm 70 \mu m^{-1}$ , respectively.





500  
 501  
 502  
 503  
 504  
 505  
 506

**FIG. 4.** Forward simulation of [002] peak at 7.5 keV. Line intensity variations from experimental data (solid blue), DM (dashed amber), AR (dashed green), and KA (dashed red) are plotted across the center of 3D diffraction intensity, along (a) y-axis and (b) x-axis of detector, and (c) rocking axis. Black error bars represent the Poisson noise of DM model simulation at  $\pm 50$  and  $\pm 70 \mu\text{m}^{-1}$ , respectively. (d) Detail of the first few orders of side lobes on the  $-\Delta q$  side, from data shown in (a) Black error bars represent the Poisson noise of DM model simulation at -20, -30, and -40  $\mu\text{m}^{-1}$ , respectively.



507  
 508  
 509  
 510  
 511

**FIG. A1.** Reconstructions from diffraction data simulated using different models. (a), (d) are retrieved from KA, (b), (e) are from AR, and (c), (f) are from DM. Traditional shrink-wrap algorithm was used when inverting (a), (b), and (c), while (d), (e), and (f) were inverted using the two-step approach described in Section II-B.